

# Anion-Regulated Hydroxysulfide Monoliths as OER/ORR/HER Electrocatalysts and their Applications in Self-Powered Electrochemical Water Splitting

Bin Wang, Cheng Tang, Hao-Fan Wang, Bo-Quan Li, Xiaoyang Cui, and Qiang Zhang\*

Trifunctional electrocatalysis for the oxygen evolution reaction, oxygen reduction reaction, and hydrogen evolution reaction constitutes the bottleneck of various sustainable energy devices and systems including rechargeable metal–air batteries and overall water splitting. Emerging macroscopically nanostructured catalysts are strongly requested for superior electrocatalytic activities and practical applications. Here, a 3D hydroxysulfide monolith with anion-regulated NiFe hydroxysulfide nanosheets is rationally proposed. With abundant active sites and unique structure, the as-obtained hydroxysulfide monolith exhibits superior electrocatalytic performance in oxygen evolution, hydrogen evolution, and oxygen reduction in alkaline electrolyte. When directly serving as electrodes, a small charge/discharge voltage gap of 0.76 V at 2.0 mA cm<sup>-2</sup> and a high peak power density of 248 mW cm<sup>-2</sup> are achieved for the liquid Zn–air batteries, and a low cell voltage of 1.62 V at 10 mA cm<sup>-2</sup> is detected for water splitting units. When two Zn–air batteries are serially connected to power the water splitting unit, bulky O<sub>2</sub> and H<sub>2</sub> bubbles are continuously generated on both the composite electrodes. This work demonstrates an effective strategy for controllable anion regulation and rational design of the 3D self-supporting hydroxysulfides, which is also enlightening for other advanced energy materials and diverse applications.

Due to the ever-increasing demands in energy and awareness of environment protection, the transition from fossil fuels to clean sustainable energy is inevitable for our modern energy system. As a consequence, the development of effective energy conversion and storage devices with a low cost, safe operation, eco-friendliness, and excellent durability is strongly considered. Among various candidates, both rechargeable Zn–air batteries<sup>[1]</sup> and water splitting units<sup>[2]</sup> have generated great expectations over the last decades. Despite the intense advances in anode, cathode, and electrolyte, these devices strongly suffer from limited energy efficiency, pronounced overpotential, and

unsatisfactory stability, which are mainly ascribed to the sluggish kinetics of oxygen evolution reaction (OER), oxygen reduction reaction (ORR), and hydrogen evolution reaction (HER) on working electrodes.<sup>[3,4]</sup> Therefore, highly active, long-term stable, low-cost, and environment friendly electrocatalysts are urgently required.<sup>[5]</sup>

To date, precious metal catalysts (such as Ir/IrO<sub>2</sub> for OER and Pt for ORR and HER) have been identified as the state-of-the-art electrocatalysts.<sup>[6]</sup> To replace the precious metal catalysts and further improve the electrocatalytic performance, various promising alternatives have been developed, such as perovskites,<sup>[7]</sup> nanocarbon-based materials,<sup>[8,9]</sup> and transition metal and their derivatives.<sup>[10–12]</sup> Among them, metal hydroxysulfides have been proposed very recently due to their remarkable activity, long durability, environmentally benign character, economic viability, tunable composition, and facile preparation.<sup>[13]</sup> The introduction of sulfur anions into metal hydroxides regulates the interaction between cations and anions via moderate anion regulation<sup>[14–16]</sup> and thereby rendering an enhanced electrocatalytic performance on hydroxysulfide catalysts.

Despite these exciting achievements, almost all (hydro)sulfides are synthesized via harsh preparation conditions (such as high temperature and/or long sulfurization time) to uniformly incorporate sulfur anions.<sup>[12,15,17,18]</sup> The crystalline phase of hydroxides is prone to be destroyed<sup>[12,15]</sup> and the resultant (hydro)sulfides trend to agglomerate into large particles<sup>[3,18]</sup> during the routine sulfurization process. Besides, the subsequent coating of powdery electrocatalysts onto a conductive substrate with additional polymeric binders and current collectors is time consuming and elaborate. More importantly, the coated catalyst layer cannot be adhered intimately on substrates and is prone to be peeled off from the electrode in gas-involved electrocatalysis, especially for OER and HER, during which the catalyst layer is continuously crashed by rapid bursting O<sub>2</sub> and H<sub>2</sub> bubbles. Therefore, the intimate growth of highly active nanoparticles on a conductive substrate, especially a 3D porous one, is highly desirable for robust integration of electrocatalyst into working devices.<sup>[19]</sup>

In this contribution, we proposed a free-standing hydroxysulfide monolith with rationally anion-regulated NiFe

Dr. B. Wang, C. Tang, H.-F. Wang, B.-Q. Li, Dr. X. Y. Cui, Prof. Q. Zhang  
Beijing Key Laboratory of Green Chemical Reaction Engineering  
and Technology  
Department of Chemical Engineering  
Tsinghua University  
Beijing 100084, China  
E-mail: zhang-qiang@mails.tsinghua.edu.cn

 The ORCID identification number(s) for the author(s) of this article can be found under <https://doi.org/10.1002/smt.201800055>.

DOI: 10.1002/smt.201800055

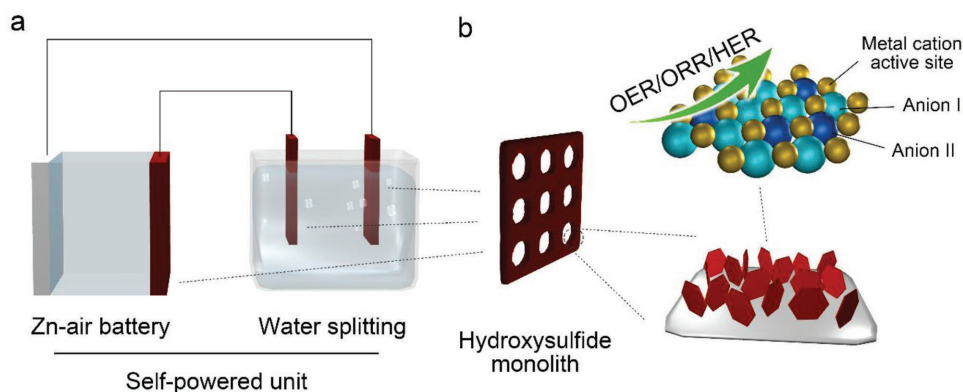


**Figure 1.** a) Schematic of the self-powered electrochemical water-splitting unit, in which NiFe hydroxysulfide monolith is directly used as air electrode for Zn–air battery, and both anode and cathode for water-splitting unit. b) The structure of the hydroxysulfide monolith electrocatalyst and the mechanism of anion regulation. The controllable introduction of anions can regulate the electronic structures of metal active sites toward highly active OER/ORR/HER in energy electrocatalysis.

hydroxysulfides that in situ uniformly grow over the 3D conductive Ni foam scaffold and explored its catalytic applications of OER, HER, and ORR in Zn–air batteries and water splitting unit (Figure 1 and Figure S1, Supporting Information). Herein, a mild sulfurization condition was employed to controllably anion-regulate the electronic structure of the hydroxysulfides. The Ni foam was employed as 3D substrates to uniformly disperse and strongly couple with the hydroxysulfide electrocatalysts. Moreover, the monolith structure, which is initially applied to treat exhaust gases of vehicle engines,<sup>[20]</sup> is supposed to reduce both the external mass transfer and internal diffusion limitations, expose large surface with active sites, uniformly distribute the flow phase, and extend catalyst lifetime.<sup>[21]</sup> As a consequence, the as-obtained composite, with balanced electronic structure, suppressed particle agglomeration, intimate interfacial coupling, interconnected electron highway, hierarchical porous channels, highly exposed active sites, and self-supporting structure, was demonstrated to exhibit excellent electrocatalytic reactivities for OER, HER, and ORR in alkaline and superior electrochemical applications in both liquid/solid Zn–air batteries and water splitting unit. Impressively, a small charge/discharge voltage gap of 0.76 V at 2.0 mA cm<sup>-2</sup> and a high peak power density of 248 mW cm<sup>-2</sup> were obtained for the liquid Zn–air battery and a low cell voltage of 1.62 V was observed at 10 mA cm<sup>-2</sup> for the water splitting unit based on this multifunctional self-supporting monolith. Further, when the water splitting unit was serially connected with two Zn–air batteries, this self-powered water splitting unit released plentiful H<sub>2</sub> and O<sub>2</sub> bubbles.

The NiFe hydroxysulfide monolith was prepared by short-time electrodeposition and controllable sulfurization procedures (Figure S1, Supporting Information). NiFe-layered double hydroxides were in situ grown on the 3D conductive Ni foam (termed as Ni<sub>2.3</sub>Fe(OH)<sub>7.6</sub>; Table S1, Supporting Information) by 60 s electrodeposition. Subsequently, the resultant monolith (termed as Ni<sub>1.9</sub>FeS<sub>1.09</sub>(OH)<sub>4.6</sub>; Table S1, Supporting information) was obtained via immersing the as-obtained Ni<sub>2.3</sub>Fe(OH)<sub>7.6</sub> precursors in a 2.0 M Na<sub>2</sub>S solution at 25 °C for 1.0 h, during which the NiFe hydroxides were controllably converted into hydroxysulfides at a very mild condition. Herein the

Ni foam (denoted as NF; Figure S2, Supporting Information) serve as a 3D conductive substrate to anchor hydroxysulfides and transfer electrons to the active sites. The hydroxysulfides uniformly disperse on the Ni foam rather than aggregate into large particles (Figure S3, Supporting Information). The application of the mild sulfurization conditions further effectively prevents the agglomeration of the as-deposited hydroxysulfides through the Ostwald ripening. As a result, the hydroxysulfides consist of an ultrathin hydroxysulfide film on the NF scaffolds with a loading amount of merely ≈0.15 mg cm<sup>-2</sup> (Figure 2a–c). The in situ growth and mild sulfurization render strong affinity between the ultrathin catalyst layer and the 3D conductive substrate, which protects the catalysts from being peeled off from the working electrode.

The hydroxysulfide nanoplates are with a typically lateral size of ≈100 nm. These nanosheets vertically interconnect and self-assemble into a 3D nanostructure that facilitates electron transfer and high exposure of active sites to the reactants. Further, the interconnected mesopores together with the macropores inside the Ni foam render a hierarchical porous structure, which benefits the rapid diffusion of electrolyte and gas during the energy electrocatalysis.

The X-ray photoelectron spectroscopy (XPS) survey spectra reveal that the S content is 3.3 at% for the NiFe hydroxysulfides and cannot be detected for the NiFe hydroxides (Figure S4, Supporting Information), revealing the successful conversion of NiFe hydroxides to corresponding hydroxysulfides. Besides, the atomic ratio of Ni to Fe is measured to be 1.9, which was in the optimized range of NiFe-based system as electrocatalysts in alkaline electrolyte.<sup>[22]</sup>

The hexagonal platelet-shape structure of hydroxides is well preserved after the controllable sulfurization process (Figure 2d and Figure S5, Supporting Information). It is quite distinct to that sulfurized under harsh conditions, during which the platelet-shape morphology of hydroxides is obviously altered.<sup>[15]</sup> The energy dispersive spectroscopy (EDS) mapping further illustrates the uniform distribution of sulfur on the hydroxysulfide nanosheets (Figure 2f). Moreover, the S is cooperated with Fe, Ni, as well as O, revealed by peak fitting of XPS spectra (Figure 2g and Figures S6–S8, Supporting Information).<sup>[23,24]</sup>

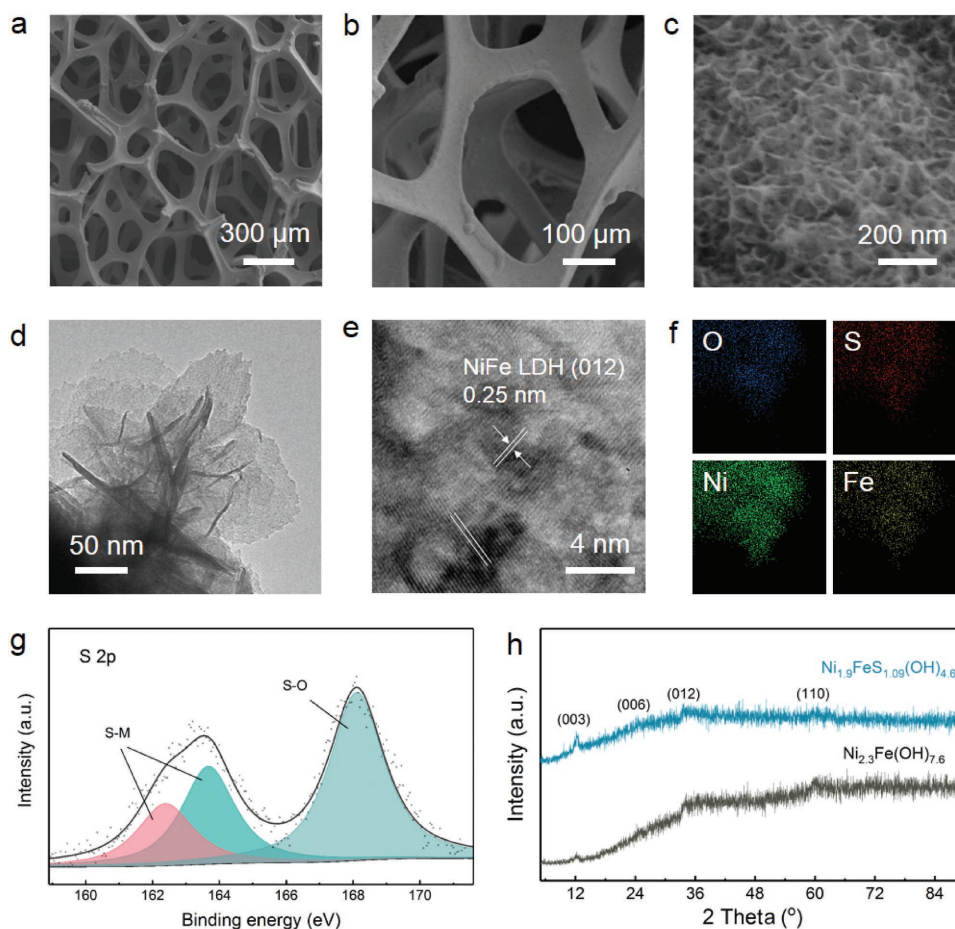


**Figure 2.** Morphology and structure characterizations of  $\text{Ni}_{1.9}\text{FeS}_{1.09}(\text{OH})_{4.6}$ . a–c) SEM images. d–f) TEM images and EDS mapping. g) XPS S 2p spectra. h) XRD pattern.

Impressively, the X-ray diffraction (XRD) pattern indicates that the as-obtained NiFe hydroxysulfides are well crystallized with a set of NiFe hydroxalite-like characteristic (003), (006), (012), and (110) peaks (Figure 2h), suggesting an R3m symmetry and hexagonal lattice.<sup>[25]</sup> Both the morphology and the crystalline phase of NiFe hydroxides are well preserved after the room temperature sulfurization process, which can be further confirmed by the lattice fringes shown in Figure 2e.<sup>[26]</sup>

Two counterpart composites with a sulfurization duration of 10 min for  $\text{Ni}_{2.1}\text{FeS}_{1.06}(\text{OH})_{5.1}$  and 40 h for  $\text{Ni}_{1.7}\text{FeS}_{1.14}(\text{OH})_{4.1}$  were also synthesized under otherwise identical conditions. The sulfur atomic content is 2.1, 3.3, and 11.0 at% for  $\text{Ni}_{2.1}\text{FeS}_{1.06}(\text{OH})_{5.1}$ ,  $\text{Ni}_{1.9}\text{FeS}_{1.09}(\text{OH})_{4.6}$ , and  $\text{Ni}_{1.7}\text{FeS}_{1.14}(\text{OH})_{4.1}$ , respectively (Table S1, Supporting Information). The scanning electron microscopy (SEM) images (Figure S9, Supporting Information) indicate that the platelet-shape morphology of NiFe hydroxides is well preserved for both  $\text{Ni}_{2.1}\text{FeS}_{1.06}(\text{OH})_{5.1}$  and  $\text{Ni}_{1.7}\text{FeS}_{1.14}(\text{OH})_{4.1}$ , which is in accordance with that of  $\text{Ni}_{1.9}\text{FeS}_{1.09}(\text{OH})_{4.6}$ . However, no strong XRD peak is observed for  $\text{Ni}_{1.7}\text{FeS}_{1.14}(\text{OH})_{4.1}$  (Figure S10, Supporting Information), indicating that the NiFe hydroxide crystalline is almost converted to an amorphous structure when the sulfurization duration is too long. The moderate sulfurization duration plays a key role for a favorable regulation of the electronic structure for active

sites. The electrocatalytic performance of  $\text{Ni}_{1.9}\text{FeS}_{1.09}(\text{OH})_{4.6}$  monolith and other control samples was investigated in a standard three-electrode system in alkaline solution (0.10 M KOH). **Figure 3a** records the iR-corrected linear sweep voltammetry (LSV) polarization curves for OER. The peaks around 1.43 V (vs RHE) are assigned to the  $\text{Ni}^{2+}/\text{Ni}^{3+}$  redox current and partly overlap with the OER current, which are decoupled via employing the chronoamperometric method (Figures S11 and S12, Supporting Information).<sup>[27]</sup>  $\text{Ni}_{1.9}\text{FeS}_{1.09}(\text{OH})_{4.6}$  monolith exhibits the best electrocatalytic activities for both OER and HER (Figure 3a–d).  $\text{Ni}_{1.9}\text{FeS}_{1.09}(\text{OH})_{4.6}$  outperforms the precious Ir/C catalyst with a small onset potential negatively shifted more than 80 mV (Figure 3a and Figure S11, Supporting Information). The overpotential required for 10  $\text{mA cm}^{-2}$  ( $\eta_{10}$ )<sup>[11,28]</sup> is reduced by 69 mV for OER (Figure 3a and Figure S12, Supporting Information). Moreover,  $\text{Ni}_{1.9}\text{FeS}_{1.09}(\text{OH})_{4.6}$  delivers a small Tafel slope of 53  $\text{mV dec}^{-1}$ , which is even slightly lower than Ir/C (56  $\text{mV dec}^{-1}$ ), revealing  $\text{Ni}_{1.9}\text{FeS}_{1.09}(\text{OH})_{4.6}$  as an excellent OER catalyst with rapid kinetics for OER.<sup>[24]</sup> Likewise, the Tafel slope of  $\text{Ni}_{1.9}\text{FeS}_{1.09}(\text{OH})_{4.6}$  for HER is 97  $\text{mV dec}^{-1}$  (Figure 3d), which is obviously lower than that of the precious Pt/C catalyst (106  $\text{mV dec}^{-1}$ ). As a result, the faster kinetics of  $\text{Ni}_{1.9}\text{FeS}_{1.09}(\text{OH})_{4.6}$  induces a dramatically boosted current density. The HER current density of 80  $\text{mA cm}^{-2}$  is achieved at an

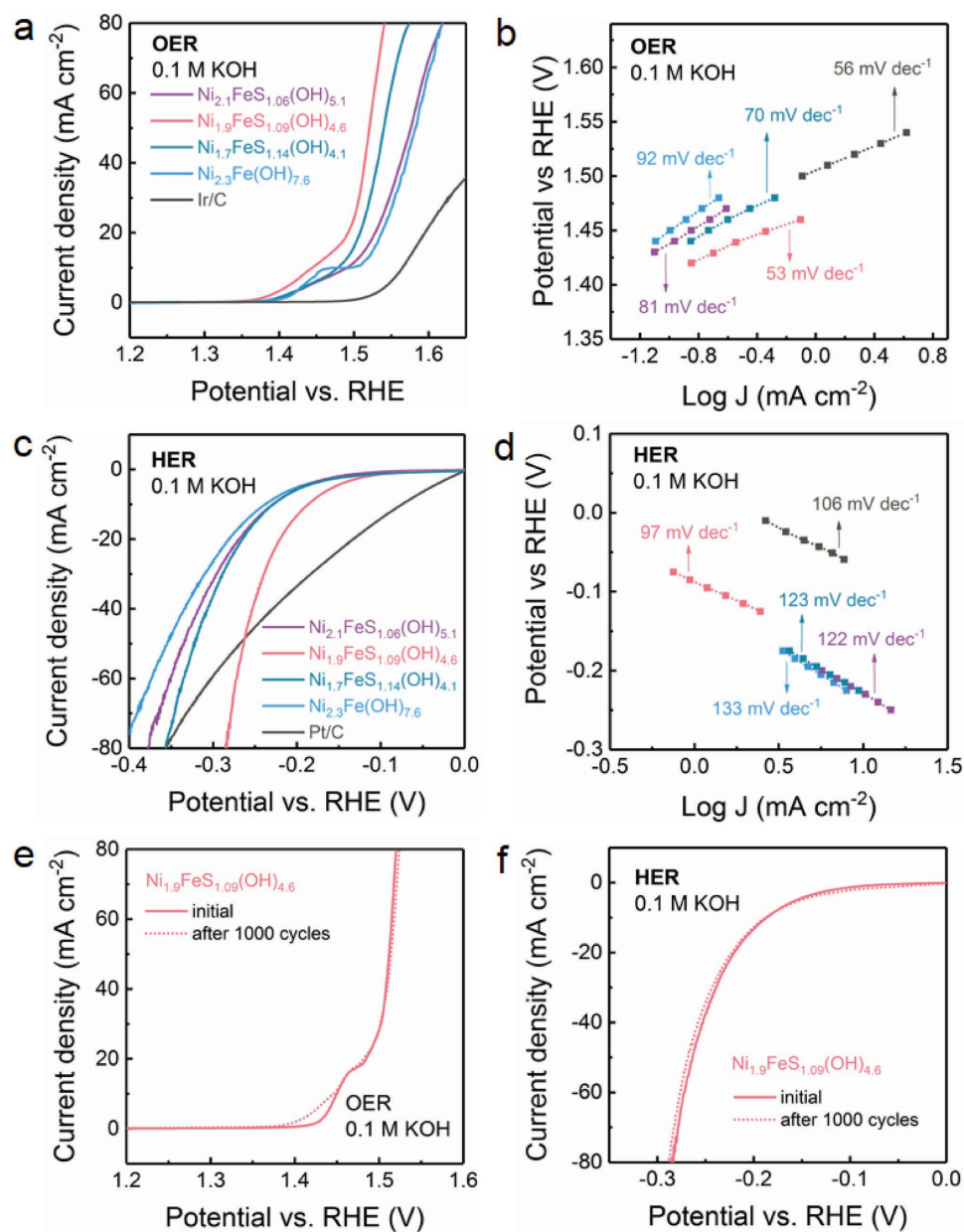


**Figure 3.** The OER and HER performance of  $\text{Ni}_{2.3}\text{Fe}(\text{OH})_{7.6}$ ,  $\text{Ni}_{2.1}\text{FeS}_{1.06}(\text{OH})_{5.1}$ ,  $\text{Ni}_{1.9}\text{FeS}_{1.09}(\text{OH})_{4.6}$ ,  $\text{Ni}_{1.7}\text{FeS}_{1.14}(\text{OH})_{4.1}$ , and precious metal catalysts. a) OER LSV plots. b) OER Tafel plots. c) HER LSV plots. d) HER Tafel plots. e) OER LSV recorded for  $\text{Ni}_{1.9}\text{FeS}_{1.09}(\text{OH})_{4.6}$  before and after 1000 cycles of CV scan. f) HER LSV recorded for  $\text{Ni}_{1.9}\text{FeS}_{1.09}(\text{OH})_{4.6}$  before and after 1000 cycles of CV scan.

overpotential of 276 mV, which is more than 1.5-fold that of the state-of-the-art Pt/C catalyst (Figure 3c). Additionally, the  $\text{Ni}_{1.9}\text{FeS}_{1.09}(\text{OH})_{4.6}$  monolith also exhibits excellent long-term durability for OER and HER, implied by the nearly overlapped LSV curves after 1000 cyclic voltammetry (CV) cycles (Figure 3e,f). Notably, the morphology and structure are well preserved after the long-term test (Figures S11–S13, Supporting Information), further proving the excellent stability of this composite. Besides,  $\text{Ni}_{1.9}\text{FeS}_{1.09}(\text{OH})_{4.6}$  monolith also exhibits the largest electrochemical active surface (Figure S14, Supporting Information) and the lowest resistance among all samples (Figures S15 and S16, Supporting Information), which benefit the mass and electron transfer and lead to higher catalytic activity.

The  $\text{Ni}_{2.3}\text{Fe}(\text{OH})_{7.6}$  sample displays a higher OER/HER activity than the bare Ni foam, with  $\eta_{10}$  reduced by 104 mV for OER and 68 mV for HER (Figure 3a–d and Figures S17–S19, Supporting Information). This indicates that the hydroxide layer on the NF significantly enhances the OER and HER reactivity. Moreover, the OER/HER activity is further improved after the sulfurization treatment, revealed by more than 10 mV decreased  $\eta_{10}$  and lower Tafel slope for all sulfurization-treated samples ( $\text{Ni}_{2.1}\text{FeS}_{1.06}(\text{OH})_{5.1}$ ,  $\text{Ni}_{1.9}\text{FeS}_{1.09}(\text{OH})_{4.6}$ , and  $\text{Ni}_{1.7}\text{FeS}_{1.14}(\text{OH})_{4.1}$ ) than those for  $\text{Ni}_{2.3}\text{Fe}(\text{OH})_{7.6}$  in both OER and HER tests. The introduction of sulfur anions facilitates OER and HER on hydroxysulfide electrocatalysts. Notably,  $\text{Ni}_{2.1}\text{FeS}_{1.06}(\text{OH})_{5.1}$ ,  $\text{Ni}_{1.9}\text{FeS}_{1.09}(\text{OH})_{4.6}$ , and  $\text{Ni}_{1.7}\text{FeS}_{1.14}(\text{OH})_{4.1}$

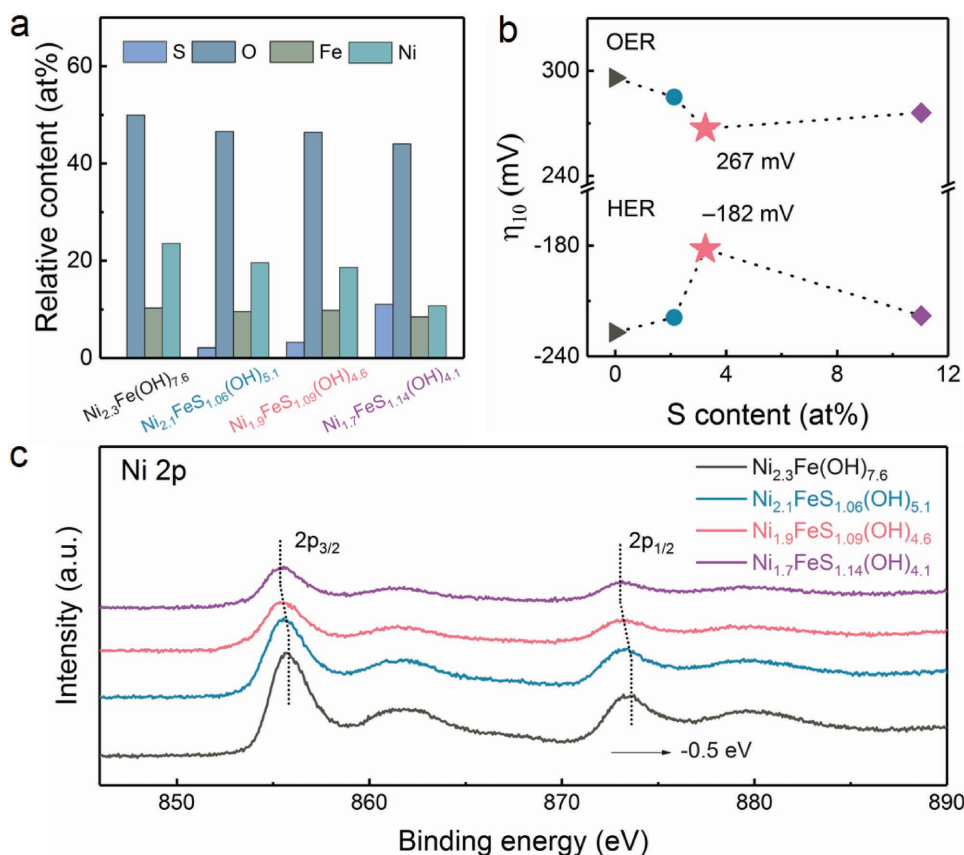


**Figure 4.** The influence of sulfurization degree on the elemental composition and OER/HER reactivity of corresponding hydroxysulfides. a) Atomic relative content of S, O, Fe, and Ni in different samples. b) OER/HER reactivity at an overpotential at 10 mA cm<sup>-2</sup>. c) High-resolution Ni 2P XPS spectra.

exhibit distinct current density and Tafel slopes among each other, implying that the sulfurization degree is crucial to the electrocatalytic performance for the hydroxysulfides. Moreover, the ORR peak currents for the sulfurized samples are larger than that of  $\text{Ni}_{2.3}\text{Fe}(\text{OH})_{7.6}$  and are different with each other as well (Figure S20, Supporting Information). This further confirms the significant importance of sulfurization and sulfurization degree to the hydroxysulfides for energy electrocatalysis.

Figure 4a further demonstrates the influence of the sulfurization degree on the compositions. The metal compositions can relatively keep stable with a similar NiFe atomic content when the sulfurization time is short (less than 1 h) and the sulfurization degree is low. Besides, the sulfur content increases from 0 ( $\text{Ni}_{2.3}\text{Fe}(\text{OH})_{7.6}$ ), 2.1 at% ( $\text{Ni}_{2.1}\text{FeS}_{1.06}(\text{OH})_{5.1}$ ) to 3.25 at% ( $\text{Ni}_{1.9}\text{FeS}_{1.09}(\text{OH})_{4.6}$ ), while the oxygen content reduces from 49.9 at% ( $\text{Ni}_{2.3}\text{Fe}(\text{OH})_{7.6}$ ), 46.6 at% ( $\text{Ni}_{2.1}\text{FeS}_{1.06}(\text{OH})_{5.1}$ ) to 46.4 at% ( $\text{Ni}_{1.9}\text{FeS}_{1.09}(\text{OH})_{4.6}$ ), suggesting a gradual substitution of hydroxides by sulfides during the sulfurization process. With the introduction of a small amount of sulfur anions, both the OER and HER activities are prominently enhanced. Compared with  $\text{Ni}_{2.3}\text{Fe}(\text{OH})_{7.6}$ ,  $\text{Ni}_{2.1}\text{FeS}_{1.06}(\text{OH})_{5.1}$  delivers an  $\eta_{10}$  reduced by 11 mV for OER and 8 mV for HER. Further,  $\text{Ni}_{1.9}\text{FeS}_{1.09}(\text{OH})_{4.6}$  outperforms  $\text{Ni}_{2.1}\text{FeS}_{1.06}(\text{OH})_{5.1}$  with  $\eta_{10}$  decreased by 18 mV for OER and 37 mV for HER, suggesting a further improved OER and HER activity by increasing sulfur anions.  $\text{Ni}_{1.7}\text{FeS}_{1.14}(\text{OH})_{4.1}$ , the one with the highest sulfur

content of 11.0 at%, however, delivers inferior OER and HER activity than  $\text{Ni}_{1.9}\text{FeS}_{1.09}(\text{OH})_{4.6}$ , with  $\eta_{10}$  increased by 9 mV for OER and 36 mV for HER, suggesting a negative effect of high-degree sulfurization on electrocatalysis. Additionally, the CV curves in ORR experiments exhibit similar tendency over the sulfurization of hydroxysulfides (Figure S20, Supporting Information), with  $\text{Ni}_{1.9}\text{FeS}_{1.09}(\text{OH})_{4.6}$  exhibiting a more positive onset potential and larger ORR peak current than  $\text{Ni}_{2.1}\text{FeS}_{1.06}(\text{OH})_{5.1}$  and  $\text{Ni}_{1.7}\text{FeS}_{1.14}(\text{OH})_{4.1}$ .

The electronic structure of the metal cations is highly dependent on their adjacent anions.<sup>[16,29]</sup> Therefore, both electronegativity and polarization of anions have a dramatically impact on the electronic structure of active cations and thus crucial to the electrocatalytic performance.<sup>[15,30]</sup> The anions with quite high electronegativity hold their electrons tightly and are hard to be polarized, thereby resulting in a too strong positive electric field of cations owing to the lack of electrons. In contrast, the anions with weak electronegativity afford too much electrons into the empty orbits of cations by polarizing and result in a deficient positive field of the cations. A reasonable electronegativity and polarization of anions is of paramount importance to render a balanced interaction between cations and anions. As for the hydroxysulfides, the NiFe components with active 3d electrons serve as the active sites for OER/HER/ORR. The oxygen ions as the dominant anions in the hydroxysulfides are hard to be polarized and thus cannot afford enough

electrons to NiFe cations. In contrast, sulfur anion processes a lower electronegativity than oxygen anion and is easier to be polarized to share more dispersed electrons with metal ions to balance the strong positive fields of NiFe ions. This can be confirmed by the shift to a lower binding energy in the high-resolution Ni 2p and Fe 2p XPS spectra due to the lowered oxidative state of NiFe elements by receiving more electrons from sulfur anions (Figure 4c and Figure S21, Supporting Information).<sup>[23]</sup> Therefore, the introduction of a moderate amount of sulfur can controllably regulate the interactions between NiFe cations and anions toward favorable electronic structures. It simultaneously facilitates the adsorption, electron transfer, and desorption process, thereby significantly enhancing the electrocatalytic reactivity of the hydroxysulfides for OER/HER/ORR. When too much sulfur anions are introduced into the hydroxysulfides, however, the balance would be destroyed again, resulting in a decreased electrocatalytic activity.

Besides the intrinsic activity of active sites, the nanostructure of the 3D composite electrocatalyst also plays a critical role to the electrocatalysis. To investigate the impact of the structure on the electrocatalytic performance for this composite, two counterpart samples with Ni<sub>1.9</sub>FeS<sub>1.09</sub>(OH)<sub>4.6</sub> powder binding to Ni foam (b Ni<sub>1.9</sub>FeS<sub>1.09</sub>(OH)<sub>4.6</sub>/NF) and carbon cloth (b Ni<sub>1.9</sub>FeS<sub>1.09</sub>(OH)<sub>4.6</sub>/CC) substrates were also fabricated, whose areal loading amount is exactly same as that of Ni<sub>1.9</sub>FeS<sub>1.09</sub>(OH)<sub>4.6</sub> monolith (0.15 mg cm<sup>-2</sup>). Compared with b Ni<sub>1.9</sub>FeS<sub>1.09</sub>(OH)<sub>4.6</sub>/NF and b Ni<sub>1.9</sub>FeS<sub>1.09</sub>(OH)<sub>4.6</sub>/CC, Ni<sub>1.9</sub>FeS<sub>1.09</sub>(OH)<sub>4.6</sub> monolith delivers an  $\eta_{10}$  reduced by more than 85 mV for OER and 47 mV for HER (Figures S18 and S22, Supporting Information). This indicates that the in situ growth of hydroxysulfide nanosheets with intimately interfacial coupling and self-assembled 3D networks dramatically enhances OER and HER reactivity. Besides, the Ni<sub>1.9</sub>FeS<sub>1.09</sub>(OH)<sub>4.6</sub> monolith also exhibits a substantially larger ORR current peak and more positive onset potential than b Ni<sub>1.9</sub>FeS<sub>1.09</sub>(OH)<sub>4.6</sub>/NF and b Ni<sub>1.9</sub>FeS<sub>1.09</sub>(OH)<sub>4.6</sub>/CC, demonstrating an improved ORR reactivity from the unique structure as well (Figure S23, Supporting Information). Contributed by the in situ growth of the hydroxysulfides and the monolith structure, Ni<sub>1.9</sub>FeS<sub>1.09</sub>(OH)<sub>4.6</sub> monolith exhibits the best electrocatalytic performance for OER/HER/ORR. The superior electrocatalytic performance of this composite does not merely arise from the hydroxysulfide active sites, but is also dependent on its indispensable structure features.

Hydroxysulfide monoliths with the self-supporting and well conductive structure can be directly used as the electrode in the energy conversion and storage devices, which avoids the elaborate procedures for the electrode fabrication and the employment of current collector and polymeric binder. Furthermore, such unique nanostructures can protect the catalyst layer from being peeled off during gas-involved electrocatalysis. To evaluate the practical applications of Ni<sub>1.9</sub>FeS<sub>1.09</sub>(OH)<sub>4.6</sub> monolith, a rechargeable liquid Zn–air battery was assembled first, with Ni<sub>1.9</sub>FeS<sub>1.09</sub>(OH)<sub>4.6</sub> as air cathode, zinc foil as anode, and 6.0 M KOH aqueous solution with 0.2 M ZnCl<sub>2</sub> as electrolyte. The mixture of the commercial state-of-the-art Pt/C for ORR and Ir/C for OER (denoted as Pt/C + Ir/C) was employed as the control catalyst.

As shown in Figure 5a, when cycled at 2.0 mA cm<sup>-2</sup>, the Zn–air battery based on Ni<sub>1.9</sub>FeS<sub>1.09</sub>(OH)<sub>4.6</sub> air cathode delivers an

initial discharge voltage of 1.14 V and a charge voltage of 1.90 V. The voltage gap is only 0.76 V and the round-trip efficiency is as high as 60%, which are even superior to those of Pt/C + Ir/C (a voltage gap of 1.01 V and a round-trip efficiency of 53%), demonstrating superb OER/ORR activity and rechargeability in a working Zn–air battery. After a 25 h test for 75 cycles, the initial charge–discharge voltage gap is well maintained (Figure S24, Supporting Information), suggesting an excellent long-term stability. Besides, the Zn–air battery catalyzed by Ni<sub>1.9</sub>FeS<sub>1.09</sub>(OH)<sub>4.6</sub> air cathode delivers a much higher discharge current density and a prominently shrunken charge–discharge voltage gap than the one based on Pt/C + Ir/C (Figure 5b), further conforming the superior activity and rechargeability of Ni<sub>1.9</sub>FeS<sub>1.09</sub>(OH)<sub>4.6</sub> monolith. Impressively, the peak power density for the battery catalyzed by Ni<sub>1.9</sub>FeS<sub>1.09</sub>(OH)<sub>4.6</sub> is as high as 248 mW cm<sup>-2</sup>, nearly fivefold that of Pt/C + Ir/C. These remarkable metrics are among the best results ever reported (Table S2, Supporting Information).<sup>[8,12,31]</sup>

Based on the excellent liquid battery performance, Ni<sub>1.9</sub>FeS<sub>1.09</sub>(OH)<sub>4.6</sub> monolith was also directly applied as the air cathode to obtain a flexible solid-state rechargeable Zn–air battery, coupled with zinc foil anode and alkaline poly (vinyl alcohol) gel electrolyte. When cycled at 2.0 mA cm<sup>-2</sup>, this battery delivers a stable charge (1.80 V) and discharge (0.77 V) voltage even at different bending angles (Figure 5c). A low voltage gap of 1.03 V is obtained on this solid battery. It is noteworthy that the alkaline gel electrolyte is prone to react with the CO<sub>2</sub> in the atmosphere, which negatively affects the long-term stability. The replacement of the gel electrolyte by fresh ones is prerequisite to obtain a long-term stability for the flexible Zn–air batteries working in atmosphere. The powdery electrocatalysts coated on the current collector, however, are prone to be stuck to the sticky gel electrolyte, especially for the binder-coated ones (Figure S25a, Supporting Information), resulting in a significant degradation of cell performance after refreshing the gel electrolyte. Impressively, a virtually unchanged discharge and charge potential is observed after replacing the gel electrolyte for the flexible Zn–air battery catalyzed by Ni<sub>1.9</sub>FeS<sub>1.09</sub>(OH)<sub>4.6</sub> air electrode, which is due to the strong binding between the hydroxysulfides and the Ni foam substrate in Ni<sub>1.9</sub>FeS<sub>1.09</sub>(OH)<sub>4.6</sub> monolith (Figure S25b, Supporting Information).

Besides excellent OER/ORR activity, Ni<sub>1.9</sub>FeS<sub>1.09</sub>(OH)<sub>4.6</sub> also possesses impressive HER performance. The efficient electrocatalysis for HER coupled with OER is crucial for hydrogen production by water splitting. To investigate the water splitting performance of Ni<sub>1.9</sub>FeS<sub>1.09</sub>(OH)<sub>4.6</sub>, a two-electrode system (Figure S26, Supporting Information) was used in N<sub>2</sub>-saturated 1.0 M KOH at room temperature (25 °C), with Ni<sub>1.9</sub>FeS<sub>1.09</sub>(OH)<sub>4.6</sub> monolith as both anode and cathode directly. As shown in Figure 5d, a much negatively shifted onset potential and prominently higher current density are observed for Ni<sub>1.9</sub>FeS<sub>1.09</sub>(OH)<sub>4.6</sub> in comparison with those of the precious Pt/C + Ir/C catalyst. The voltage at 10 mA cm<sup>-2</sup> is determined as low as 1.62 V, reduced by 190 mV than that of Pt/C + Ir/C, demonstrating a superior water splitting performance for Ni<sub>1.9</sub>FeS<sub>1.09</sub>(OH)<sub>4.6</sub>, which is among the best results ever reported (Table S3, Supporting Information).<sup>[32]</sup>

Further, encouraged by the excellent performance of both Zn–air batteries and water splitting, two liquid Zn–air batteries

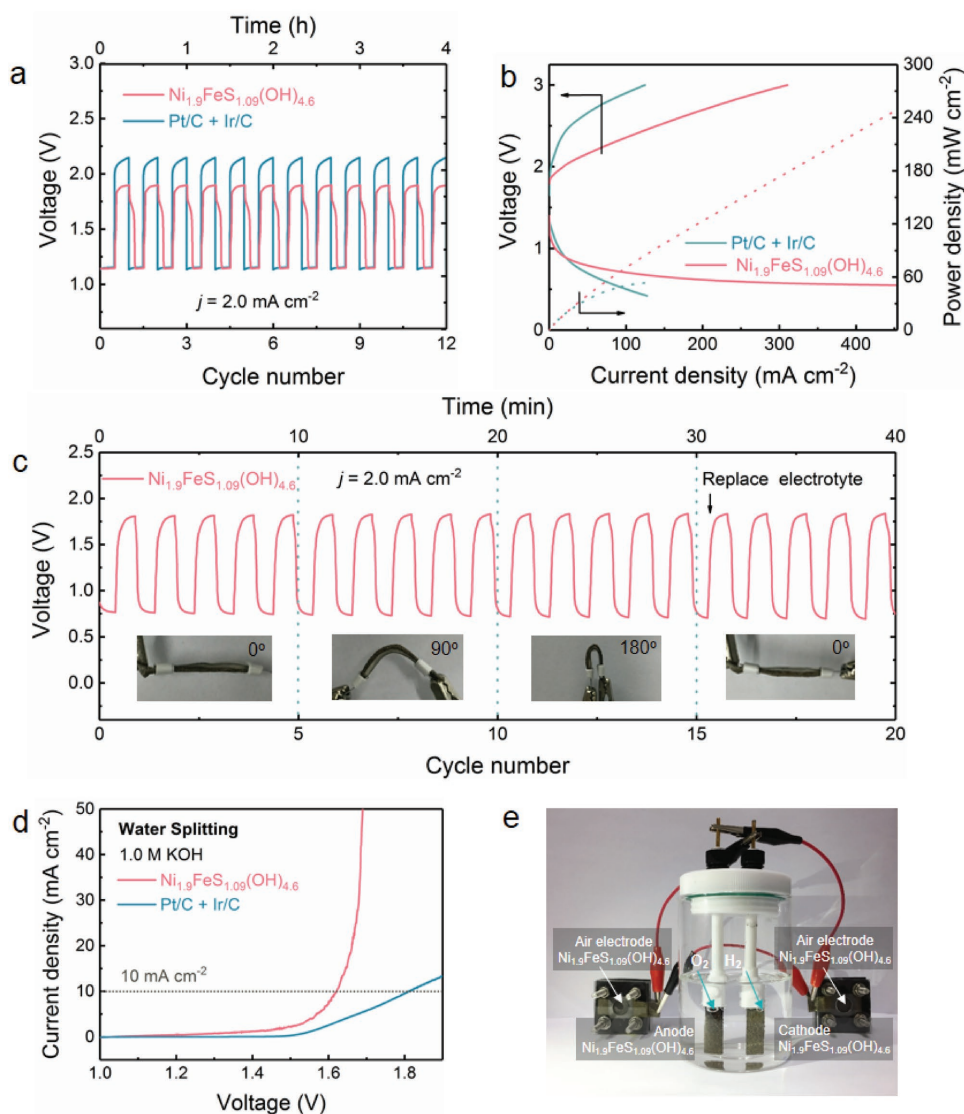


**Figure 5.** Applications of  $\text{Ni}_{1.9}\text{FeS}_{1.09}(\text{OH})_{4.6}$  monolith. a) Galvanostatic discharge–charge cycling curves and b) charge and discharge polarization curves of rechargeable liquid Zn–air batteries. c) Galvanostatic discharge–charge cycling curves under bending of the flexible rechargeable Zn–air batteries. d) LSV profiles for overall water splitting in  $\text{N}_2$ -saturated 1.0 M KOH. e) Self-powered water-splitting unit driven by two-series-connected liquid Zn–air batteries.

catalyzed by  $\text{Ni}_{1.9}\text{FeS}_{1.09}(\text{OH})_{4.6}$  were serially connected to the water splitting unit using  $\text{Ni}_{1.9}\text{FeS}_{1.09}(\text{OH})_{4.6}$  as both cathode and anode, with 1.0 M KOH solution as electrolyte at room temperature (25 °C). Owing to the excellent OER/ORR/HER activity, bulky  $\text{O}_2$  and  $\text{H}_2$  bubbles are continuously generated on the  $\text{Ni}_{1.9}\text{FeS}_{1.09}(\text{OH})_{4.6}$  anode and cathode, respectively (Figure 5e).

The NiFe hydroxysulfide monoliths fabricated by in situ growth and rational anionic regulation are systematically demonstrated to exhibit an enhanced intrinsic reactivity for OER/HER/ORR and promising applications in both liquid and flexible solid rechargeable Zn–air batteries, and water splitting unit. It is ascribed to the following intrinsic advantages: (1) the reasonable sulfur anion regulation facilitating the optimization of the electronic structure and increase of intrinsic reactivity; (2) the effectively prevented aggregation of hydroxysulfide products during growth and sulfidization; (3) the hierarchical

porous architecture with large pores inside the substrate and mesopores generated from hydroxysulfides facilitating rapid gas and electrolyte diffusion; and (4) the strong coupled interface between hydroxysulfides and conductive substrates for enhanced electron transportation and protected catalyst layer from being peeled off.

In summary, a self-supported NiFe hydroxysulfide monolith electrocatalyst is proposed and facilely fabricated via a two-step synthetic strategy for trifunctional OER/HER/ORR electrocatalysis. On the one hand, the controllable anion regulation by moderate sulfurization generates highly active sites in the hydroxysulfides. On the other hand, the monolithic Ni foam serves as 3D substrate to uniformly disperse and strongly couple with the vertically interconnected hydroxysulfide nanosheets. Consequently, the as-obtained hydroxysulfide monolith electrocatalyst affords highly exposed active sites,

abundant porous channels, intimate interfacial coupling, interconnected electron highway, and self-supporting feature, facilitating the gas-involved OER/HER/ORR energy electrocatalysis. Contributed by the highly active sites and unique structure, this composite exhibits impressive OER/HER/ORR reactivity and promising performance in both liquid and flexible solid-state rechargeable Zn–air batteries and water splitting units. The OER activity outperforms that of Ir/C, with an overpotential of 266 mV at 10 mA cm<sup>-2</sup> ( $\eta_{10}$ ) and a small Tafel slope of 53 mV dec<sup>-1</sup>. The Tafel slope for HER is only 97 mV dec<sup>-1</sup>, prominently smaller than that of Pt/C (106 mV dec<sup>-1</sup>). This composite with the free-standing and 3D conductive structure can be directly applied as working electrodes in the energy conversion and storage devices. The flexible solid Zn–air battery catalyzed by the composite gives a stable discharge (0.77 V) and charge (1.80 V) voltage at 2.0 mA cm<sup>-2</sup> at different bending angles and after refreshing the gel electrolyte. The liquid rechargeable Zn–air battery based on the NiFe hydroxysulfide monolith delivers a low charge/discharge voltage gap of 0.76 V at 2.0 mA cm<sup>-2</sup> and a high peak power density of 248 mW cm<sup>-2</sup>, outperforming those of commercial state-of-the-art Pt/C and Ir/C mixture (a charge/discharge gap of 1.01 V and a peak power density of 53 mW cm<sup>-2</sup>). The cell voltage at 10 mA cm<sup>-2</sup> for the water splitting unit with this composite as both electrodes is determined as low as 1.62 V, much smaller than that of Pt/C and Ir/C mixture (1.81 V). This work demonstrates an emerging smart material design concept and effective synthetic strategy for the anion-regulated self-supporting hydroxysulfide monoliths, which is an emerging advanced energy material aiming at highly effective energy electrocatalysis in a family of energy conversion and storage devices.

## Supporting Information

Supporting Information is available from the Wiley Online Library or from the author.

## Acknowledgements

This work was supported by the National Key Research and Development Program (Grant Nos. 2016YFA0202500 and 2016YFA0200102), the National Natural Scientific Foundation of China (Grant Nos. 21676160 and 21706146), and the China Postdoctoral Science Foundation (Grant No. 2016M600097).

## Conflict of Interest

The authors declare no conflict of interest.

## Keywords

anion regulation, electrochemical water splitting, nanostructured electrocatalysts, oxygen evolution/reduction reactions, Zn–air batteries

Received: February 20, 2018  
Revised: March 11, 2018  
Published online: May 4, 2018

- [1] a) D. Yang, L. Zhang, X. Yan, X. Yao, *Small Methods* **2017**, *1*, 1700209; b) J. Fu, Z. P. Cano, M. G. Park, A. Yu, M. Fowler, Z. Chen, *Adv. Mater.* **2017**, *29*, 1604685; c) J.-S. Lee, S. Tai Kim, R. Cao, N.-S. Choi, M. Liu, K. T. Lee, J. Cho, *Adv. Energy Mater.* **2011**, *1*, 34; d) Y. Li, H. Dai, *Chem. Soc. Rev.* **2014**, *43*, 5257.
- [2] a) L. Han, S. Dong, E. Wang, *Adv. Mater.* **2016**, *28*, 9266; b) B. M. Hunter, H. B. Gray, A. M. Müller, *Chem. Rev.* **2016**, *116*, 14120; c) X. Zou, Y. Zhang, *Chem. Soc. Rev.* **2015**, *44*, 5148; d) J. Wang, W. Cui, Q. Liu, Z. Xing, A. M. Asiri, X. Sun, *Adv. Mater.* **2016**, *28*, 215; e) Y. Hou, X. Zhuang, X. Feng, *Small Methods* **2017**, *1*, 1700090.
- [3] L. Zhou, M. Shao, C. Zhang, J. Zhao, S. He, D. Rao, M. Wei, D. G. Evans, X. Duan, *Adv. Mater.* **2017**, *29*, 1604080.
- [4] a) W. Zhang, W. Lai, R. Cao, *Chem. Rev.* **2017**, *117*, 3717; b) Y. Zhang, Q. Zhou, J. Zhu, Q. Yan, S. X. Dou, W. Sun, *Adv. Funct. Mater.* **2017**, *27*, 1702317; c) X.-Y. Yu, L. Yu, X. W. Lou, *Small Methods* **2017**, *1*, 1600020.
- [5] a) Y. Jiao, Y. Zheng, M. Jaroniec, S. Z. Qiao, *Chem. Soc. Rev.* **2015**, *44*, 2060; b) N.-T. Suen, S.-F. Hung, Q. Quan, N. Zhang, Y.-J. Xu, H. M. Chen, *Chem. Soc. Rev.* **2017**, *46*, 337.
- [6] a) Y. Nie, L. Li, Z. Wei, *Chem. Soc. Rev.* **2015**, *44*, 2168; b) J. Feng, F. Lv, W. Zhang, P. Li, K. Wang, C. Yang, B. Wang, Y. Yang, J. Zhou, F. Lin, G.-C. Wang, S. Guo, *Adv. Mater.* **2017**, *29*, 1703798.
- [7] a) B.-Q. Li, Z.-J. Xia, B. Zhang, C. Tang, H.-F. Wang, Q. Zhang, *Nat. Commun.* **2017**, *8*, 934; b) B. Q. Li, C. Tang, H. F. Wang, X. L. Zhu, Q. Zhang, *Sci. Adv.* **2016**, *2*, e1600495.
- [8] C. Tang, B. Wang, H.-F. Wang, Q. Zhang, *Adv. Mater.* **2017**, *29*, 1703185.
- [9] a) J. Zhang, Z. Zhao, Z. Xia, L. Dai, *Nat. Nanotechnol.* **2015**, *10*, 444; b) C. Tang, H.-F. Wang, X. Chen, B.-Q. Li, T.-Z. Hou, B. Zhang, Q. Zhang, M.-M. Titirici, F. Wei, *Adv. Mater.* **2016**, *28*, 6845; c) G.-L. Tian, M.-Q. Zhao, D. Yu, X.-Y. Kong, J.-Q. Huang, Q. Zhang, F. Wei, *Small* **2014**, *10*, 2251; d) T. Y. Ma, J. Ran, S. Dai, M. Jaroniec, S. Z. Qiao, *Angew. Chem., Int. Ed.* **2015**, *54*, 4646; e) H. B. Yang, J. Miao, S.-F. Hung, J. Chen, H. B. Tao, X. Wang, L. Zhang, R. Chen, J. Gao, H. M. Chen, *Sci. Adv.* **2016**, *2*, e1501122; f) C. Hu, L. Dai, *Adv. Mater.* **2017**, *29*, 1604942; g) M. Zhou, H.-L. Wang, S. Guo, *Chem. Soc. Rev.* **2016**, *45*, 1273; h) X. Zhang, X. Cheng, Q. Zhang, *J. Energy Chem.* **2016**, *25*, 967; i) D. Yan, Y. Li, J. Huo, R. Chen, L. Dai, S. Wang, *Adv. Mater.* **2017**, *29*, 1606459; j) C. Tang, M.-M. Titirici, Q. Zhang, *J. Energy Chem.* **2017**, *26*, 1077.
- [10] a) X. Zou, Y. Liu, G.-D. Li, Y. Wu, D.-P. Liu, W. Li, H.-W. Li, D. Wang, Y. Zhang, X. Zou, *Adv. Mater.* **2017**, *29*, 1700404; b) Z. Zhao, H. Wu, H. He, X. Xu, Y. Jin, *Adv. Funct. Mater.* **2014**, *24*, 4698; c) M. S. Burke, M. G. Kast, L. Trotochaud, A. M. Smith, S. W. Boettcher, *J. Am. Chem. Soc.* **2015**, *137*, 3638; d) X. Lu, C. Zhao, *Nat. Commun.* **2015**, *6*, 6616; e) C. Tang, L. Zhong, B. Zhang, H.-F. Wang, Q. Zhang, *Adv. Mater.* **2018**, *30*, 1705110; f) L. Zhou, M. Shao, M. Wei, X. Duan, *J. Energy Chem.* **2017**, *26*, 1094.
- [11] C. C. McCrory, S. Jung, J. C. Peters, T. F. Jaramillo, *J. Am. Chem. Soc.* **2013**, *135*, 16977.
- [12] H.-F. Wang, C. Tang, B. Wang, B.-Q. Li, Q. Zhang, *Adv. Mater.* **2017**, *29*, 1702327.
- [13] a) J. Yang, G. Zhu, Y. Liu, J. Xia, Z. Ji, X. Shen, S. Wu, *Adv. Funct. Mater.* **2016**, *26*, 4712; b) P. Cai, J. Huang, J. Chen, Z. Wen, *Angew. Chem., Int. Ed.* **2017**, *56*, 4858.
- [14] J. Duan, S. Chen, A. Vasileff, S. Z. Qiao, *ACS Nano* **2016**, *10*, 8738.
- [15] B.-Q. Li, S.-Y. Zhang, C. Tang, X. Cui, Q. Zhang, *Small* **2017**, *13*, 1700610.
- [16] G. Wan, C. Yang, W. Zhao, Q. Li, N. Wang, T. Li, H. Zhou, H. Chen, J. Shi, *Adv. Mater.* **2017**, *29*, 1703436.
- [17] A. Ishikawa, T. Takata, J. N. Kondo, M. Hara, H. Kobayashi, K. Domen, *J. Am. Chem. Soc.* **2002**, *124*, 13547.
- [18] J. Fu, F. M. Hassan, C. Zhong, J. Lu, H. Liu, A. Yu, Z. Chen, *Adv. Mater.* **2017**, *29*, 1702526.
- [19] C. Tang, H.-F. Wang, Q. Zhang, *Acc. Chem. Res.* **2018**, *51*, 881.
- [20] J. L. Williams, *Catal. Today* **2001**, *69*, 3.

- [21] G. Groppi, E. Tronconi, *Chem. Eng. Sci.* **2000**, *55*, 2161.
- [22] a) M. W. Louie, A. T. Bell, *J. Am. Chem. Soc.* **2013**, *135*, 12329; b) J. Y. C. Chen, J. T. Miller, J. B. Gerken, S. S. Stahl, *Energy Environ. Sci.* **2014**, *7*, 1382; c) D. Friebel, M. W. Louie, M. Bajdich, K. E. Sanwald, Y. Cai, A. M. Wise, M.-J. Cheng, D. Sokaras, T.-C. Weng, R. Alonso-Mori, R. C. Davis, J. R. Bargar, J. K. Nørskov, A. Nilsson, A. T. Bell, *J. Am. Chem. Soc.* **2015**, *137*, 1305; d) C. Tang, H.-F. Wang, H.-S. Wang, F. Wei, Q. Zhang, *J. Mater. Chem. A* **2016**, *4*, 3210.
- [23] B. You, Y. Sun, *Adv. Energy Mater.* **2016**, *6*, 1502333.
- [24] Y. Sun, C. Liu, D. C. Grauer, J. Yano, J. R. Long, P. Yang, C. J. Chang, *J. Am. Chem. Soc.* **2013**, *135*, 17699.
- [25] C. Tang, H. S. Wang, H. F. Wang, Q. Zhang, G. L. Tian, J. Q. Nie, F. Wei, *Adv. Mater.* **2015**, *27*, 4516.
- [26] a) M. Gong, Y. Li, H. Wang, Y. Liang, J. Z. Wu, J. Zhou, J. Wang, T. Regier, F. Wei, H. Dai, *J. Am. Chem. Soc.* **2013**, *135*, 8452; b) X. Zhu, C. Tang, H.-F. Wang, B.-Q. Li, Q. Zhang, C. Li, C. Yang, F. Wei, *J. Mater. Chem. A* **2016**, *4*, 7245.
- [27] a) X. Zhu, C. Tang, H.-F. Wang, Q. Zhang, C. Yang, F. Wei, *J. Mater. Chem. A* **2015**, *3*, 24540; b) H.-F. Wang, C. Tang, Q. Zhang, *J. Mater. Chem. A* **2015**, *3*, 16183.
- [28] M. G. Walter, E. L. Warren, J. R. McKone, S. W. Boettcher, Q. Mi, E. A. Santori, N. S. Lewis, *Chem. Rev.* **2010**, *110*, 6446.
- [29] P. Chen, T. Zhou, M. Zhang, Y. Tong, C. Zhong, N. Zhang, L. Zhang, C. Wu, Y. Xie, *Adv. Mater.* **2017**, *29*, 1701584.
- [30] A. Grimaud, W. T. Hong, Y. Shao-Horn, J. M. Tarascon, *Nat. Mater.* **2016**, *15*, 121.
- [31] a) S. Li, C. Chen, X. Zhao, J. Schmidt, A. Thomas, *Angew. Chem., Int. Ed.* **2018**, *57*, 1856; b) L. Wei, H. E. Karahan, S. Zhai, H. Liu, X. Chen, Z. Zhou, Y. Lei, Z. Liu, Y. Chen, *Adv. Mater.* **2017**, *29*, 1701410; c) P. Chen, T. Zhou, L. Xing, K. Xu, Y. Tong, H. Xie, L. Zhang, W. Yan, W. Chu, C. Wu, Y. Xie, *Angew. Chem., Int. Ed.* **2017**, *56*, 610.
- [32] a) J. Yin, Y. Li, F. Lv, M. Lu, K. Sun, W. Wang, L. Wang, F. Cheng, Y. Li, P. Xi, S. Guo, *Adv. Mater.* **2017**, *29*, 1704681; b) M.-S. Balogun, W. Qiu, Y. Huang, H. Yang, R. Xu, W. Zhao, G.-R. Li, H. Ji, Y. Tong, *Adv. Mater.* **2017**, *29*, 1702095; c) Y. Xu, W. Tu, B. Zhang, S. Yin, Y. Huang, M. Kraft, R. Xu, *Adv. Mater.* **2017**, *29*, 1605957; d) L. Fang, W. Li, Y. Guan, Y. Feng, H. Zhang, S. Wang, Y. Wang, *Adv. Funct. Mater.* **2017**, *27*, 1701008; e) X. Gao, H. Zhang, Q. Li, X. Yu, Z. Hong, X. Zhang, C. Liang, Z. Lin, *Angew. Chem., Int. Ed.* **2016**, *55*, 6290.